Journal Name

Electronic Supplementary Information ESI

Electronic Supplementary Information ESI

Received 00th January 20xx,
Accepted 00th January 20xx

DOI: 10.1039/x0xx00000x

www.rsc.org/

Platinum for hydrogen sensing: surface and grain boundary scattering antagonistic effects in Pt@Au core-shell nanoparticle assemblies prepared by Langmuir-Blodgett†.

K. Rajouâ[a], L. Baklouti[a] and F. Favier[a]

UV-Visible spectroscopy

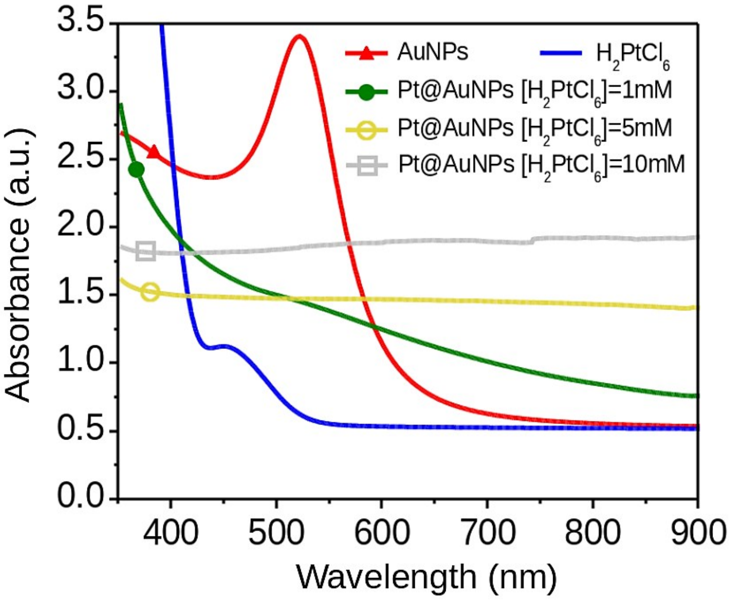

Fig. S1 UV-visible spectra of a 5 mM H_2PtCl_6 solution (blue solid line) and gold nanoparticles (red solid triangle), and Pt@Au colloids from 1 mM (green solid circle), 5 mM (yellow open circle) and 10 mM (grey open square) H_2PtCl_6 solutions.

Fig. S1 depicts the UV-Visible spectra of Au colloids suspension (red solid triangle), H_2PtCl_6 solution at 5 mM concentration (blue solid line) and Pt@Au nanoparticles suspensions prepared respectively from 1 mM (green solid circle), 5 mM (yellow open circle) and 10 mM (grey open square) H_2PtCl_6 solutions. The Au nanoparticles suspension spectrum (red solid triangle) shows a band at 520 nm characteristic of the surface plasmonic resonance of gold colloids in the visible range (Fig. 1a).[1] The adsorption of ascorbic acid (Fig. 1b) leads to the same spectrum than raw gold colloids. However, this band is no longer observed in the spectra of the prepared Pt@Au nanoparticle suspensions (Fig. S1) since the formation of platinum shells at the gold surface disrupts the surface plasmonic resonance phenomenon. Moreover, in the spectrum

---

[a] Institut Charles Gerhardt de Montpellier UMR 5253 CNRS, University of Montpellier, Campus Triolet, cc1502, 34095 Montpellier cedex 05, France, E-Mail: khalil.rajoua@univ-montp2.fr, frederic.favier@univ-montp2.fr, Tel: +33467143332.

of the H_2PtCl_6 solution (blue solid line), the absorption peak at 448 nm, characteristic of the d-d transition of Pt^{4+}, disappears in Pt@Au nanoparticles suspension spectra as a proof of the full consumption of the Pt precursor salt.

TEM micrographs of nanoparticles

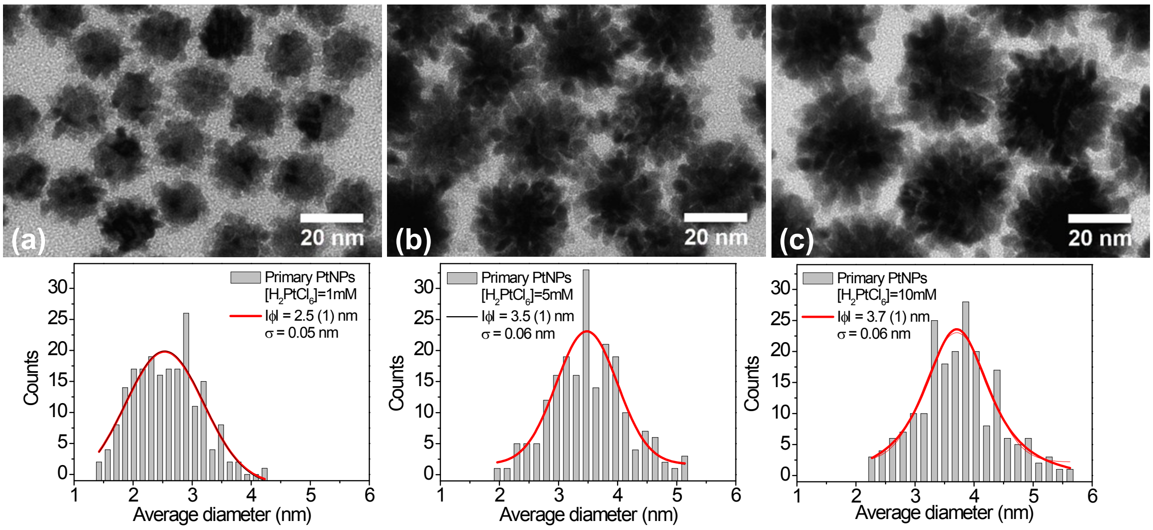

Fig. S2 TEM micrographs and particle size distributions of Pt@Au core-shell nanoparticles magnify (x150k) on shells with $[H_2PtCl_6]$ = 1 mM **(a)**, $[H_2PtCl_6]$ = 5 mM **(b)**, and $[H_2PtCl_6]$ = 10 mM **(c)**.

Platinum nanoparticles forming the shells have a spherical morphology and an average diameter of 2.5 (1) nm (Fig. S2a), 3.5 (1) nm (Fig. S2b) and 3.7 (1) nm (Fig. S2c) depending on the initial precursor concentration, 1 mM, 5 mM and 10 mM, respectively. Their size distributions are quite narrow as they spread from 1.4 nm to 4.2 nm for particles from 1 mM precursor concentration ($\Delta_{\emptyset}$ = 2.8 nm and σ = 0.7 nm), from 1.9 nm to 5.2 nm for particles from 5 mM precursor concentration ($\Delta_{\emptyset}$ = 3.3 nm and σ = 0.5 nm) and from 2.2 nm to 5.7 nm for particles from 10 mM precursor concentration ($\Delta_{\emptyset}$ = 3.5 nm and σ = 0.5 nm).

X-Ray Diffraction

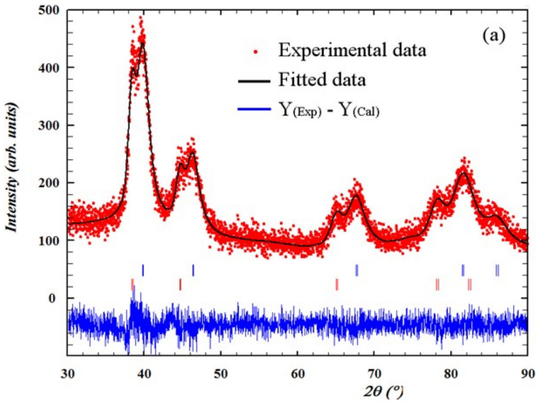

(a)

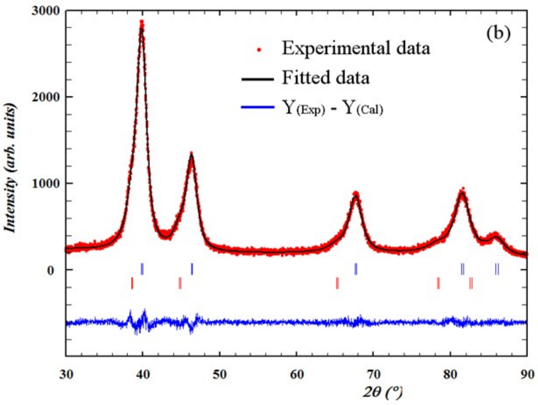

(b)

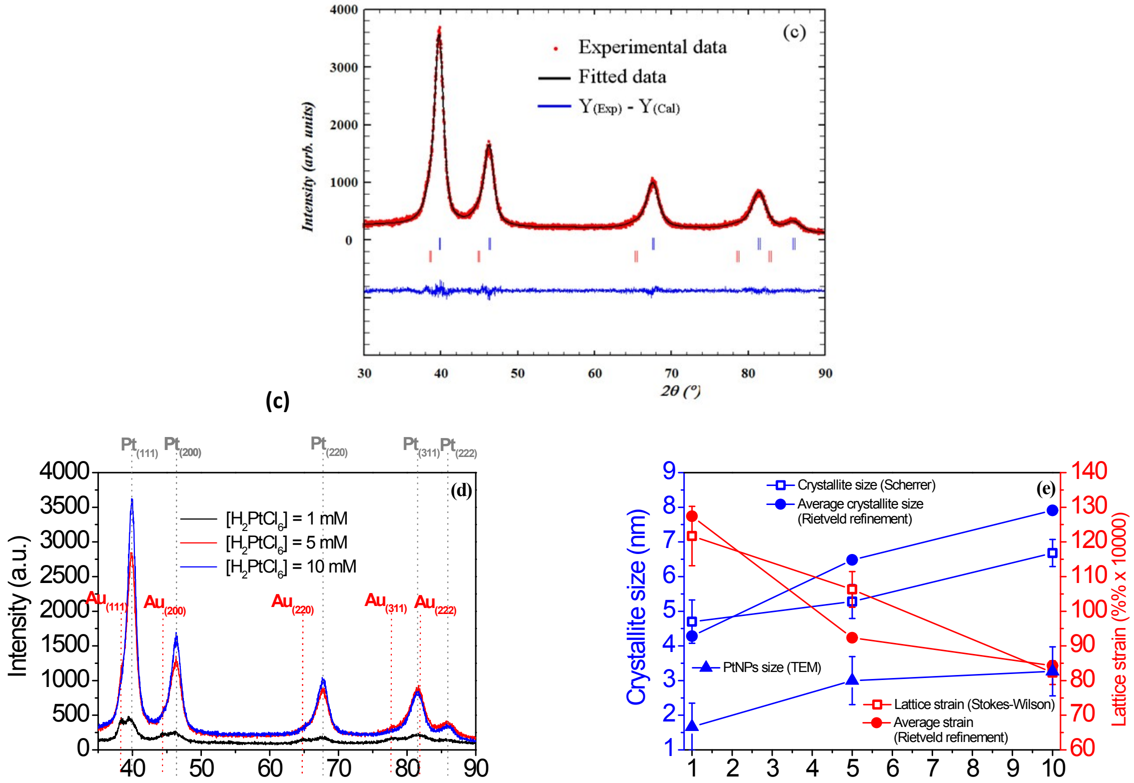

(c)

(d) (e)

Fig. S3 XRD diffractogram of Pt@Au nanoparticles (red symbols), simulated data obtained by the Rietveld method (black curves), and the difference between the both curves Y_{Exp} - Y_{Cal} (blue curves) for particles from the various platinum precursor concentration: $[H_2PtCl_6]$ = 1 mM **(a)**, 5 mM **(b)**, and 10 mM **(c)**. Superposition of the diffractograms of the three kinds of nanoparticles **(d)**. Average crystallite size Lv and lattice strain ε obtains from the two routes (Scherrer and Stokes-Wilson calculation and Rietveld refinement by Fullprof) are represented in **(e)**.

The Fig. S3d depicts the raw XRD diffractograms of the different Pt@Au core-shell nanoparticles from various platinum precursor concentrations: $[H_2PtCl_6]$ = 1 mM, 5 mM and 10 mM. In the series, peak positions and relative intensities are characteristic of gold (card n° 052249 of ICSD) and platinum (card n° 064923 of ICSD) diffractive material.

The Scherrer relationship was used to determine the crystallite size **(5)**, and the Stokes-Wilson equation to determine the lattice strains **(6)**:[2-5]

$$Lv = \frac{K\lambda}{\beta \times \cos\theta}$$ Scherrer equation **(5)**

$$\varepsilon = \frac{\beta}{4 \times \tan\theta}$$ Stokes-Wilson equation **(6)**

with $$\varepsilon = \frac{\beta \times \cos\theta - \dfrac{K \times \lambda}{Lv}}{4 \times \sin\theta}$$ Williamson-Hall equation **(7)**

With:

- Lv is the mean size of the ordered crystalline domains or average crystallite size (Å)
- ε is the lattice strain (%)
- K is a shape factor, K = 0.9 for isotropic crystallite
- λ is the X-ray wavelength (Å), $\lambda_{CuK\alpha}$ = 1.54056 Å
- β is the full width at half maximum intensity, β = FWHM (radians)

- θ is the Bragg angle (peak position).

The “FullProf” software was used to extract from the XRD data the average crystallite size Lv and the average maximum strain ε for each component (Pt and Au). In fact, the Rietveld method allows simulating diffractogram including peaks of the two phases.[6, 7] Thus the simulated diffractogram (black curves in the Fig. S3a, S3b and S3c) is fitted to the experimental data (red curves in the Figures S3a, S3b and S3c) by the refinements of various parameters (including Lv, ε, and the cell parameter a). The best refinement corresponds to the best fit between experimental and calculated patterns. Y_{exp}-Y_{cal}, represented by the blue curves in Fig. S3a, S3b and S3c for particles from Pt precursor concentration of 1 mM, 5 mM and 10 mM respectively, show the pattern agreements. The instrumentals broadening contribution is introduced by the refinement of the XRD diffractogram of yttrium oxide Y_2O_3, used as reference material.

	TEM	Relations		Rietveld refinement by Fullprof	
Pt@Au [H_2PtCl_6]	Particles size φ (nm)	Crystallite size **Lv** (nm) Scherrer	Lattice strain **ε** (%) Stokes-Wilson	Average apparent crystallite size **Lv** (nm)	Average maximum strain **ε** (%% (x 10000))
1 mM					
PtNPs	2.5	4.7	0.0228	4.3 (0.02)	127.4 (0.03)
Au core	12.0	11.7	0.0095	11.7 (0.03)	98.71 (0.03)
5 mM					
PtNPs	3.5	5.3	0.0201	6.5 (0.05)	92.4 (0.03)
Au core	12.0	--------	--------	11.7 (0.03)	264.9 (0.05)
10 mM					
PtNPs	3.7	6.7	0.0159	7.9 (0.02)	84.3 (0.05)
Au core	12.0	--------	--------	11.2 (0.05)	240.7 (0.05)

Table S1 Average crystallite size Lv and average maximum strain ε obtain from the two method described previously (Scherrer and Stokes-Wilson equation and Rietveld refinement).

The crystallite size Lv and the lattice strains ε calculated by the two different methods are depicted in the Fig. S3e and listed in Table S1. The gold core crystallite size is estimated at about 11.5 nm by the Rietveld refinements in the whole series of prepared core-shell materials (i.e. for the particles from 1, 5 and 10 mM Pt precursor concentration). It was measured at 12 nm by TEM. The slight difference between these two values is within the margin of error introduced by measurement and calculation errors. For the platinum shells, crystallite sizes are given in the Table S1 and plotted in the Fig. S3e (crystallite size by the Scherrer relationship in blue open squares and in blue closed circles from Rietveld refinements). On the other hand, lattice strains are represented in Fig. S3e by the red open squares from calculation using the Stokes-Wilson relation and the red closed circles by Rietveld refinement decrease with the platinum precursor concentration. For comparison, Pt particle sizes from TEM measurements are also plotted in Fig. S3e as blue closed triangles.

SEM-EDX: SEM coupled to energy-dispersive X-Ray spectroscopy microanalysis

Precursor concentration [H_2PtCl_6]	Pt (%) Atomic % (σ or SD)	Au (%) Atomic % (σ or SD)	Pt (%) Weight % (σ or SD)	Au (%) Weight % (σ or SD)
10 mM	94.2 (0.61)	5.8 (0.61)	94.1 (0.62)	5.9 (0.62)
5 mM	89.3	10.7	89.2	10.8

	(1.25)	(1.25)	(1.26)	(1.26)
1 mM	61.4 (2.12)	38.6 (2.12)	61.2 (2.13)	38.8 (2.13)

Table S2 Chemical composition of the core-shell Pt@Au nanoparticle assemblies measured by SEM-EDX. σ or standard deviation values are given in parenthesis together with the atomic or weight percentages.

The chemical composition of the Pt@Au core-shell nanoparticle assembles obtained by SEM-EDX microanalysis is given in Table S2. Either as expressed in atomic or weight percentages, when the platinum precursor concentration increases, so is the platinum rate in the shell. This point fully agrees with the linear increase of the Pt thickness, as measured from TEM imaging (Fig. S2), with the precursor concentration (Fig. S4).

Precursor concentration [H_2PtCl_6]	TEM diameter Pt@AuNPs Ø$_{TEM}$ (nm)	$R^{Cal}_{EDX} = \frac{X_{Pt}}{X_{Au}}$	$R^{Cal}_{TEM} = \frac{V_{Pt}}{V_{Au}}$	$R^{Théo}_{Vol} = \frac{V_{Pt}}{V_{Au}}$
10 mM	36.4	16.1	26.9	14.4
5 mM	28.8	8.3	12.8	7.4
1 mM	19.0	1.6	3.0	1.4

Table S3 Compositions of the different Pt shells compared to the Au shells obtained either by the chemical composition from the SEM-EDX in atomic% (R_{EDX}), or by the volume measurements from TEM (R_{TEM}), or by the theoretical way from density values (R_{Vol}).

With $$R^{Cal}_{EDX} = \frac{X_{Pt}}{X_{Au}} \quad \textbf{(8)},$$ $$R^{Cal}_{TEM} = \frac{V_{Pt}}{V_{Au}} = \frac{r^3_{Pt} - r^3_{Au}}{r^3_{Au}} \quad \textbf{(9)}$$ and $$R^{Theo}_{Vol} = \frac{V_{Pt}}{V_{Au}} = \frac{\frac{m_{Pt}}{\rho_{Pt}}}{\frac{m_{Au}}{\rho_{Au}}} = \frac{\rho_{Au}}{\rho_{Pt}} \times \frac{m_{Pt}}{m_{Au}} \quad \textbf{(10)}$$

- R^{Cal}_{EDX} : chemical atomic ratio Pt/Au from EDX measurements (atomic %)

- X_{Pt}: Pt composition in atomic % in the sensing layer

- X_{Au}: Au composition in atomic % in the sensing layer

- R^{Cal}_{TEM} : volume ratio Pt/Au calculated from TEM imaging

- V_{Pt}: volume of a Pt@Au shell nanoparticle (= $V_{Pt@Au}$ - V_{AuNP})

- V_{Au}: volume of a gold core (sphere)

- r_{Pt}: core-shell nanoparticle radius (= $r_{Pt@Au}$ - r_{AuNP})

- r_{Au}: gold nanoparticle radius

- $R^{Theo}_{Vol.}$: theoretical volume ratio from weight % measurements obtained by EDX (weight %)

- m_{Pt}: Pt composition in weight % in the nanoparticle layer

- m_{Au}: Au composition in weight % in the nanoparticle layer

- ρ_{Au}: gold density, $\rho_{Au} = 19.30$ g.cm^{-3}

- ρ_{Pt}: palladium density, $\rho_{Pt} = 21.45$ g.cm^{-3}

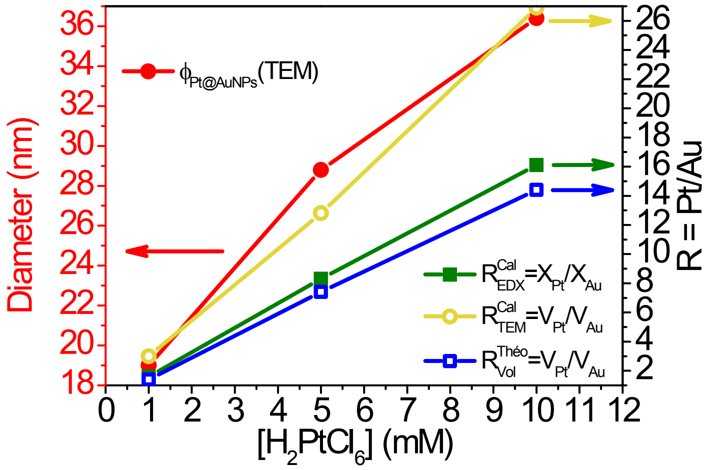

Fig. S4 Pt@Au core-shell nanoparticle diameters and the different chemical composition ratios relative to the concentration of platinum precursor.

The data in Table S3 and plotted in Fig. S4 were obtained **i/** from the SEM-EDX microanalysis in atomic % (R_{EDX} as green closed squares), **ii/** from the size measurements with TEM (R_{TEM} as yellow open circles), and **iii/** from the weight % and metal densities (R_{Vol} as blue open squares). The chemical composition ratio R_{EDX} and the volume ratio R_{Vol} are almost the same but the slight difference is caused by the errors in the EDX microanalysis.

SEM and TEM micrographs of sensing layers

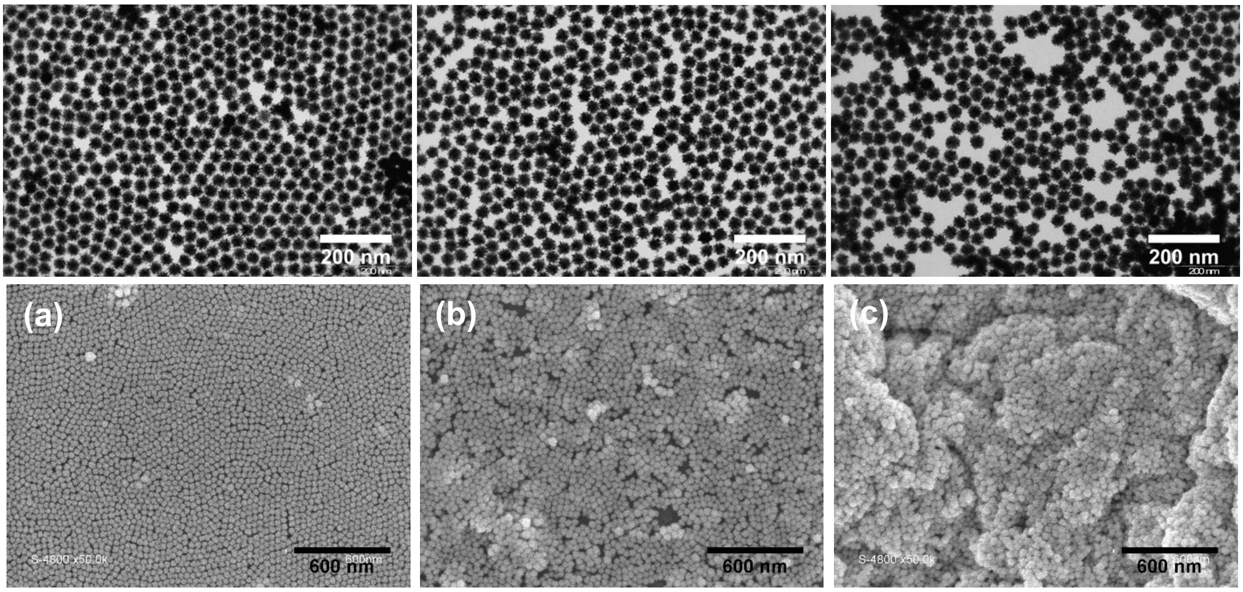

Fig. S5 TEM micrographs (top) and SEM micrographs (bottom) of Pt@Au core-shell nanoparticles assembles formed with the Langmuir-Blodgett method according to the volume of introduced ethanol during the Langmuir-Blodgett process: V_{EtOH} = 5 mL **(a)**, 7.5 mL **(b)**, and 10 mL **(c)**.

As shown in Fig. S5 by SEM and TEM, different film morphologies were obtained according to the volume of ethanol introduced during the L.B. process. The Pt@Au nanoparticles depicted in these micrographs were all synthesized from a 10 mM H_2PtCl_6 precursor solution. Only the volume of EtOH introduced was varied, at V_{EtOH} = 5 mL (Fig. S5a), 7.5 mL (Fig. S5b), and 10 mL (Fig. S5c). For less than 5 mL of introduced

EtOH, i.e. 3 mL (data not shown), a grey metallic but discontinuous film is clearly visible at naked eye. In the case of 5 mL in (Fig. S5a and Fig. 3), a dense monolayer is formed with a quasi-perfect hexagonal close packed 2D arrangement of Pt@Au nanoparticles. When the added volume of ethanol reaches 7.5 mL (Fig. S5b), multilayer islands of particles and deconstructed areas appear. Finally, a resulting thick film is formed by several particles (layer) if the introduced volume is equal or above 10 mL as depicted in Fig. S5c.

Signal amplitude responses

Calculation details for $\Delta I/I_0$ and $\Delta I/\Delta I_{max}$ are given below:

$$\frac{\Delta I}{I_0} = \frac{I - I_0}{I_0} \times 100 \quad \text{and} \quad \frac{\Delta I}{\Delta I_{Max}} = \frac{I - I_0}{\left| I_{Max} - I_{0Max} \right|} \times 100 \qquad \textbf{(11)}$$

$$\frac{\Delta I}{I_0} = \frac{I - I_0}{I_0} = \frac{R_0 - R}{R} = -\frac{\Delta R}{R} \quad \text{and} \quad \frac{\Delta I}{I} = \frac{I - I_0}{I} = \frac{R_0 - R}{R_0} = -\frac{\Delta R}{R_0} \qquad \textbf{(12)}$$

With:

- I_0 = baseline current (A)
- I = current after H_2 exposition (A)
- ΔI = signal amplitude for one concentration of $H_2 = I - I_0$ (A)
- $\Delta I/I_0$ = signal amplitudes relative to the baseline current
- I_{Max} = intensity of maximum response (A)
- I_{0Max} = intensity of the baseline before the maximum response (A)
- ΔI_{Max} = signal amplitude for the maximum response = $I_{Max} - I_{0Max}$ (A)
- $\Delta I/\Delta_{IMax}$ = signal amplitudes relative to the maximum response

Response and recovery times

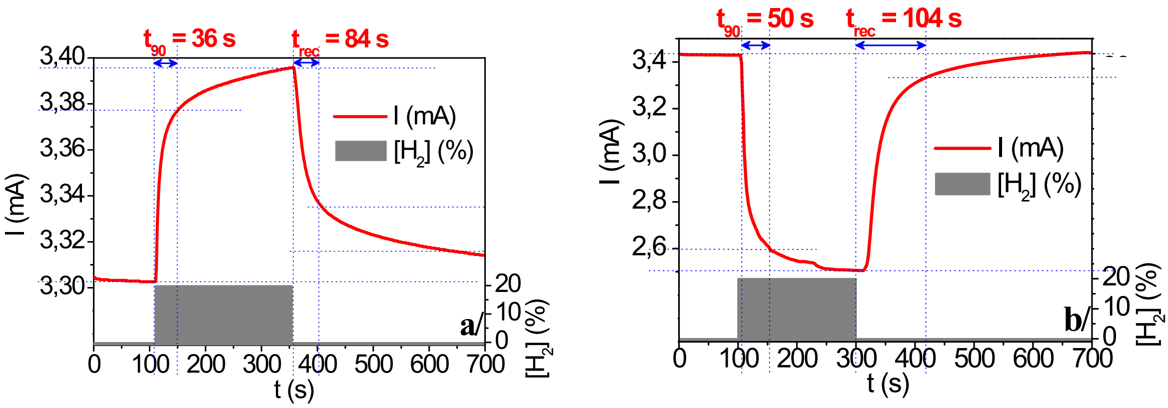

Fig. S6 Response time t_{90} and recovery time t_{rec} for Pt@Au nanoparticles for $[H_2]$ = 20% with Pt thickness at 8.4 nm **(a)** and at 12.2 nm **(b)**.

The response time t_{90} and the recovery time t_{rec} reflect the kinetic of adsorption and desorption of the different species during sensing, they are both depicted with the signal profile when exposed to a flow of 20% of hydrogen in air for the Pt@Au sensing layer with a conductive response (e_{Pt} = 8.4 nm) in the Fig. S6a and with a resistive response (e_{Pt} = 12.2 nm) in the Fig. S6b.

Sensing performances and temperature

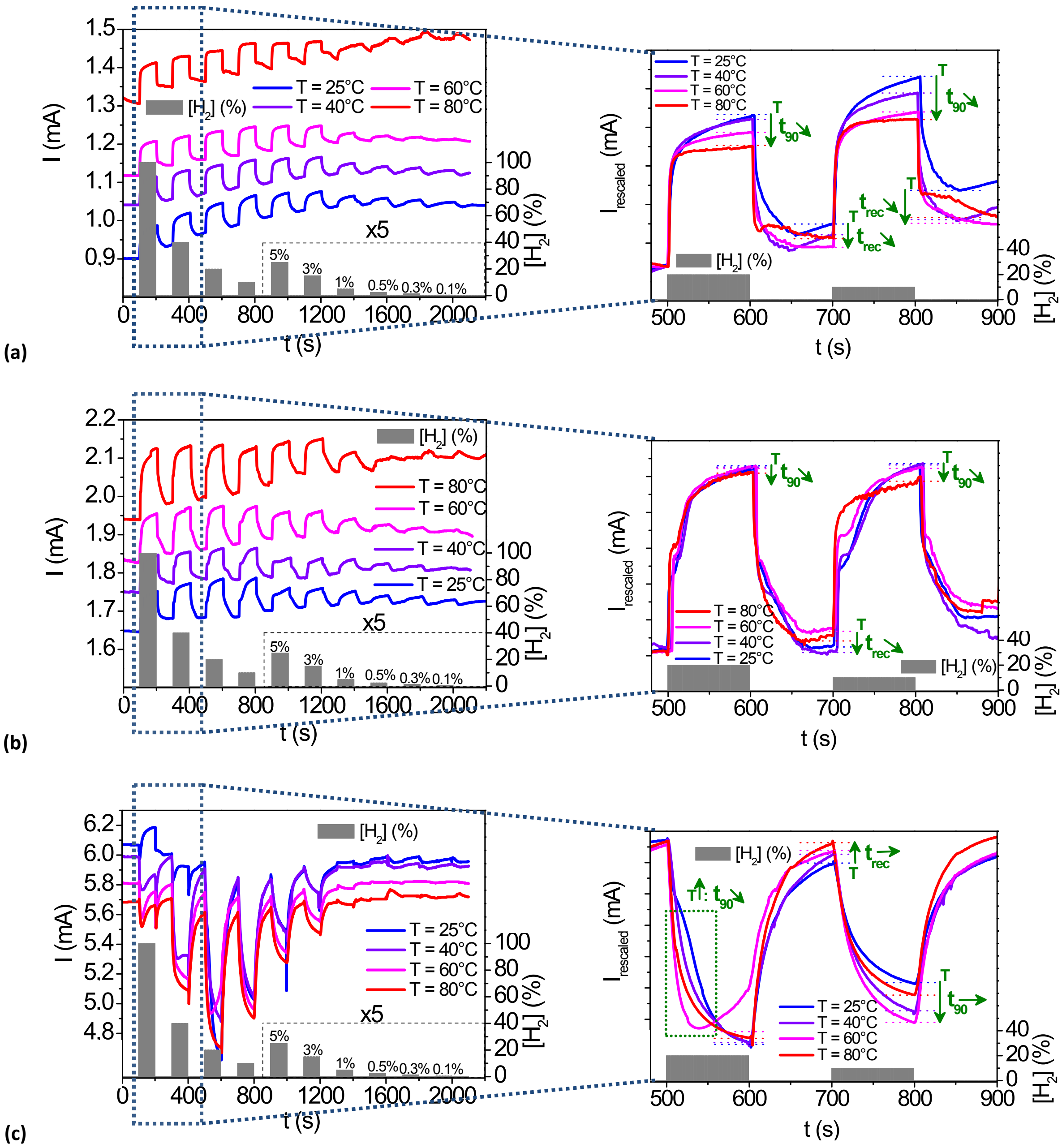

Fig. S7 Current response versus hydrogen concentration in air (grey histograms) for Pt@Au nanoparticles assembles prepared by Langmuir-Blodgett method with Pt shells at 3.5 **(a)**, 8.4 **(b)** and 12.2 nm **(c)** depending on the temperature: T = 25°C for the blue curves, 40°C for the purple curves, 60°C for the pink curves and 80°C for the red curves. Voltage bias at 0.5 V.

The Fig. S7 depicts the signal responses and the profile responses of the fabricated sensors based on Pt-shells 3.5 nm (Fig. S7a), 8.4 nm (Figure S7b) and 12.2 nm (Fig.S7c) thick at various temperature: T = 25°C (blue curves), 40°C (purple curves), 60°C (pink curves) and 80°C (red curves). The shapes and “signs” of the signal response remain for the four studied temperature: conductive and resistive responses for the thin and thick Pt shells based sensors, respectively. The baseline levels appear to increase with the temperature for the thin Pt shells as a proof of the increase of the conductivity of these sensing layers with the temperature. But this behavior is rather caused by an artifact: the drift of the baselines to the higher conductivity values during the various cycling exposition to the H_2 (especially for the highest concentrations) and air as depicted in the Fig. S7a and Fig. S7b. For the thick Pt shells represented in the Fig. S7c, the conductivity of the baselines decrease with the temperature and it is caused by the electrical metal behavior of the sensing layer: the electrical resistance of a metal increase with the temperature.

Mechanisms

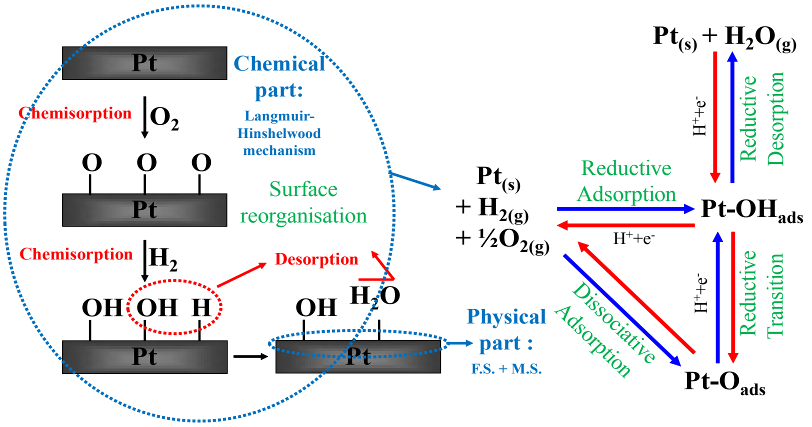

Fig. S8 Scheme of the catalytic dissociative adsorption of H_2 and O_2 on Pt by the Langmuir-Hinshelwood mechanism.

TPR and TPD of H_2 with N_2

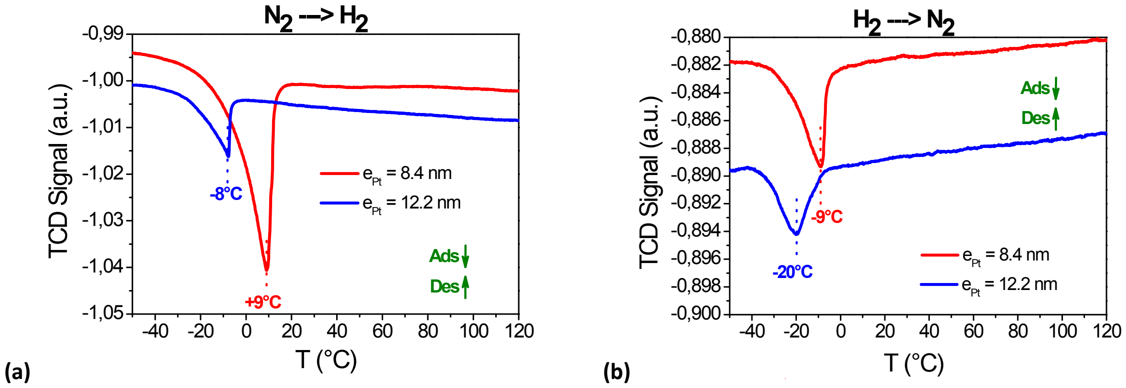

Fig. S9 Temperature Programmed Reduction TPR measurements in **(a)** on Pt@Au nanoparticles (thin shell (8.4 nm) in red and thick shell (12.2 nm) in blue) of H_2 beforehand adsorbed at -80°C and Temperature Programmed Desorption TPD measurements in **(b)** with N_2 as flushing gas. Pre-adsorption time is 5 min and the temperature rate is 10 K/min for all measurements.

Fig. S9a and S9b show the behavior of Pt@Au nanoparticles in the scanned temperature range when N_2 is flushed before or after H_2 exposure. A single adsorption peak is observed, whatever the Pt shell thickness considered for measurements. These peaks have the same profile, arise in the same temperature range and the small area under the peaks corresponds to a limited quantity of physisorbed H_2.[8]

Sensing responses and saturation

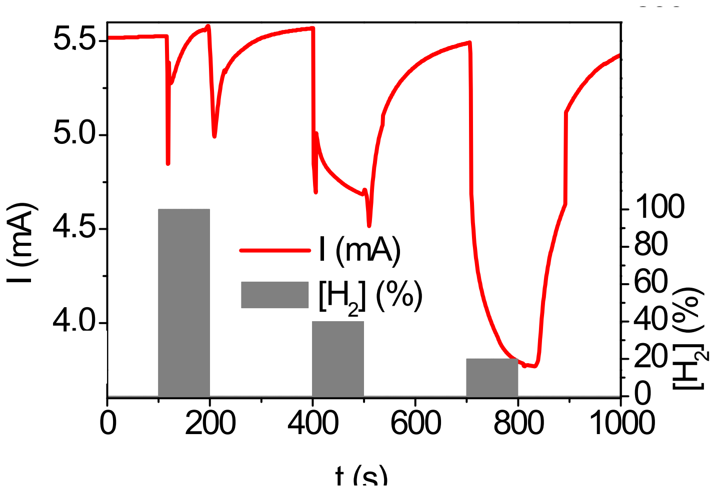

Fig. S10 Responses and saturation of sensing layer based on Pt@Au nanoparticles with thick Pt shells.

Electron scattering of conduction electron: p and Rc parameters

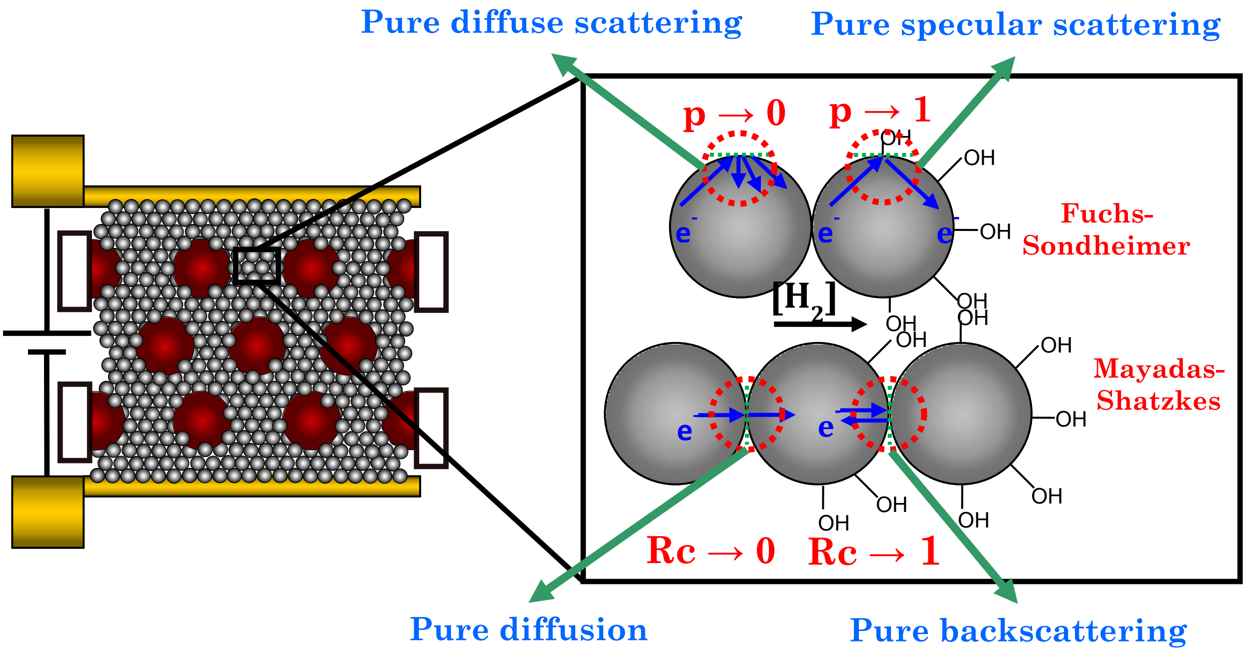

Fig. S11 Schematic representation of the conduction electron motion trough the Pt nanoparticles from Pt@Au sensing layer and their scattering on the Pt surface (Fuchs-Sondheimer theory) and at the grain boundaries (Mayadas-Shatzkes theory).

As shown in Fig. S11, for the surface, p → 0 for a pure or totally diffuse scattering (behaviour of a dispersive interface). It corresponds to a maximum resistivity variation ρ/ρ_0. In contrast, for p → 1, corresponding to a pure or totally specular scattering (behaviour of a mirror surface), there is no change in resistivity variation and $\rho/\rho_0 = 1$. At the grain boundaries, $R_c \rightarrow 0$ for a pure inelastic reflection or total diffusion and $\rho/\rho_0 = 1$, and $R_c \rightarrow 1$ for a pure elastic reflection or pure backscattering corresponding to a maximum change in resistivity variation.

Electron conduction routes in Pt@Au sensing layers

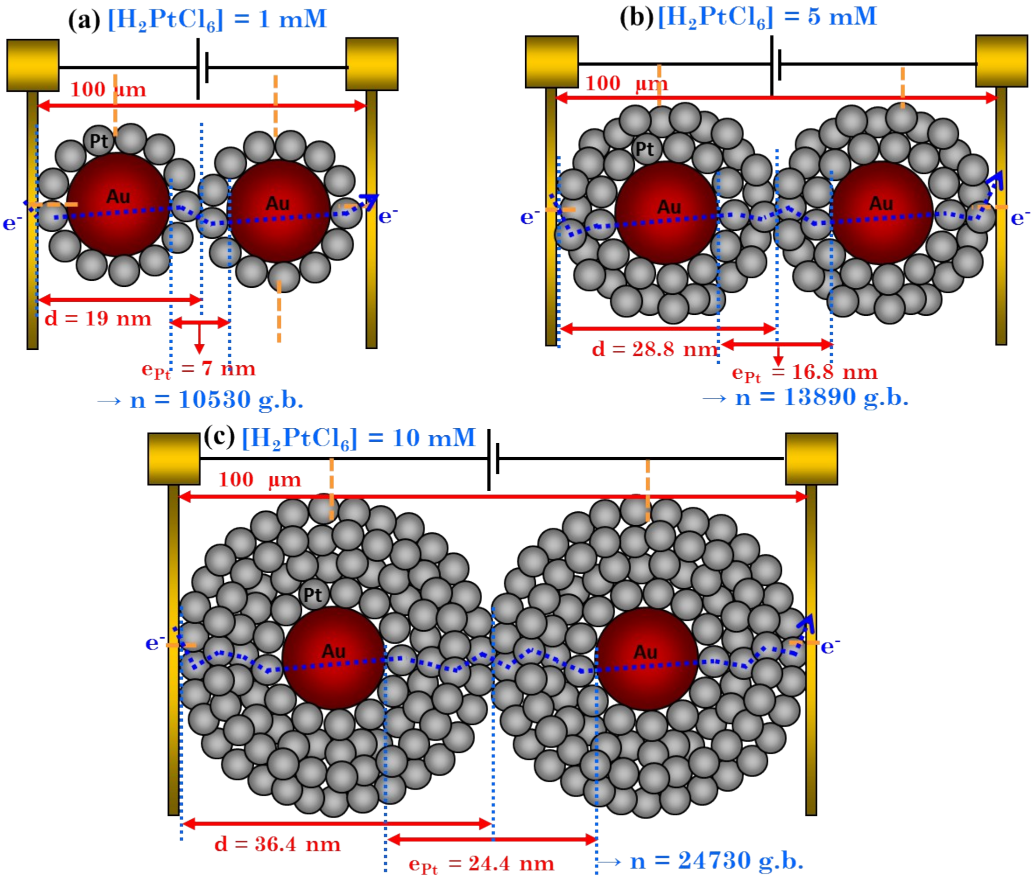

Fig. S12 Schematic representation of the size parameters and the conduction routes of the different Pt@Au core-shell nanoparticles for the different Pt thicknesses leading to the calculation of the number of grain boundaries (g.b.) involved in the Pt@Au 2D Langmuir-Blodgett monolayer of nanoparticles.

Fig. S12 depicts the conduction routes of conduction electrons through the Pt@Au core-shell nanoparticle assembles depending on the shell thickness: 3.5 nm in Fig. S12a, 8.4 nm in Fig. S12b and 12.2 nm in Fig. S12c. The number of involved grain boundaries was calculated for the shortest conduction route for a 2D hexagonal arrangement of core-shell nanoparticles. For thick Pt shells based sensors (Fig. S12c), fabricated by the Langmuir-Blodgett method (2D hexagonal monolayer), the number of grain boundaries was estimated about 24700 in the shortest conduction paths for an electrode span of 100 µm. Conversely, the number of grain boundaries was estimated about 10500 and 13900 for sensors based on thinner Pt shells at 3.5 nm and 8.4 nm as shown in Fig. S12a and S12b, respectively. p and Rc parameter values depending on the hydrogen concentration. For p and Rc calculations by using equations **(2)** or **(3)**, the following parameters were used: d corresponds to thickness of Pt shell (e_{Pt} as measured by TEM) and d_g to the average diameters of the Pt crystallites, as given in Table S4.

$[H_2PtCl_6]$ (mM)	1	5	10
e_{Pt} = d (nm)	3.5	8.4	12.2
θ_{PtNPs}(XRD refinements) = d_g (nm)	4.3	6.5	7.9

Table S4 Size parameters used for the calculation of the specular parameter (p) and the reflection coefficient (Rc) by equations (2) or (3).

p an Rc parameters evolution

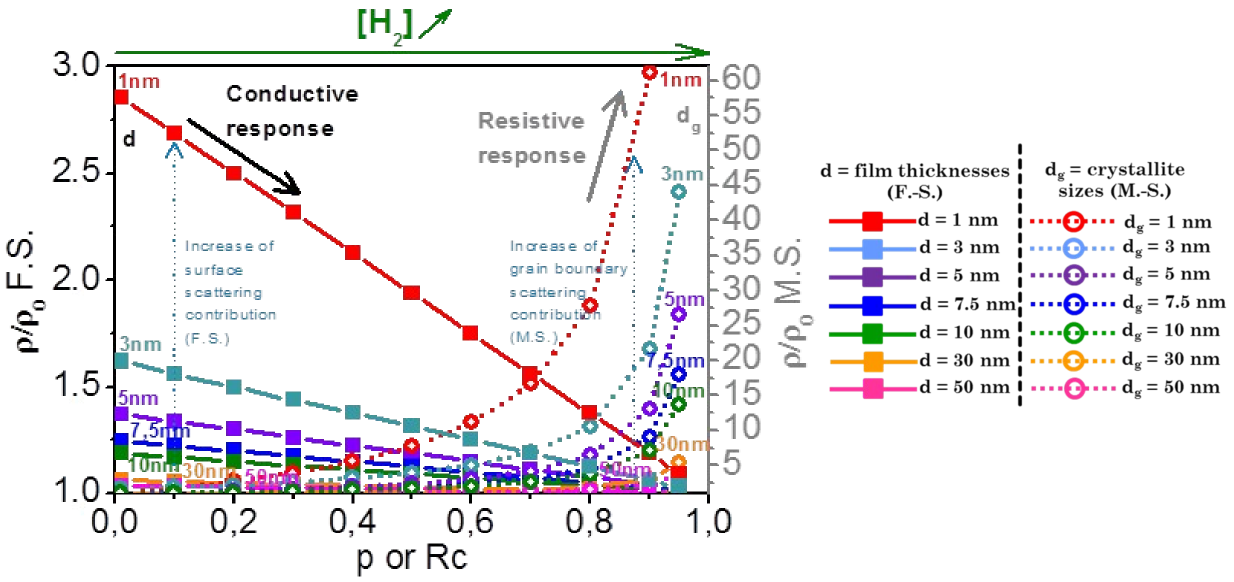

Fig. S13 Relative resistivity variation trend from the Fuchs-Sondheimer (ρ/ρ_0F.S., solid curves) and Mayadas-Shatzkes (ρ/ρ_0 M.S., dashed curves) contributions with p and Rc parameters (and correlatively, with the hydrogen concentration) for various film thicknesses d and crystallite sizes d_g, respectively.

Fig. S13 shows the resistivity variations ρ/ρ_0 against the specular parameter p used in the Fuchs-Sondheimer model in one hand and the reflection coefficient Rc used in the Mayadas-Shatzkes model in the other. They are plotted for different film thicknesses d and different crystallite sizes d_g from relation **(3)** for each contribution regardless the other. First, it can be noticed that:

- The value $\rho/\rho_0 = 1$ corresponds to the resistivity of Pt bulk: $\rho = \rho_0$.

- The values of p and Rc parameters increase with the coverage of chemisorbed species (i.e. p and Rc increase with the hydrogen concentration in air flows).

- The conductive responses correspond to curve portions with negative slopes: Since the surface scattering p increases with the hydrogen concentration, $\rho(air)/\rho_0 > \rho([H_2])/\rho_0$ and $\rho([H_2])/\rho_0$ corresponds to a negative slope. The Fuchs-Sondheimer contribution plotted as solide curves/closed squares demonstrates a linear decrease of resistivity with p.

- The resistive responses correspond to curve portions with positive slopes: Since the grain boundary scattering Rc increases with the hydrogen concentration, thus $\rho(air)/\rho_0 < \rho([H_2])/\rho_0$ and $\rho([H_2])/\rho_0$ corresponds to a positive slope. The Mayadas-Shatzkes contribution plotted as dashed curves/open circles shows that the resistivity hyperbolically increases with Rc.

Moreover, ρ/ρ_0 values calculated by M.S. can be greater than those by F.S. (see Fig. S13 y axes), as they range from 0 to 60 and 1 to 3, respectively. Consequently, sensors with resistive responses are expected to show larger amplitude responses than those with conductive responses. This point is in agreement with the sensing measurements (Fig. 4 and S6a):

- if the shell thickness d (or e_{Pt}) decreases, the contribution of the surface scattering as calculated by the F.S. model (closed squares) is greater than that from grain boundary scattering and leads to conductive responses under H_2/air exposure.

- if the nanoparticle (crystallite) size d_g decreases, the contribution of the grain boundary scattering as calculated by the M.S. model (open circles) is greater than that from surface scattering and leads to resistive responses under H_2/air exposure.

Notes and references

1. S. K. Ghosh and T. Pal, *Chemical Reviews*, 2007, **107**, 4797-4862.
2 P. Scherrer, *Nachrichten von der Gesellschaft der Wissenschaften zu Göttingen, mathematisch-physikalische Klasse*, 1918, **1918**, 98-100.
3. A. Stokes and A. Wilson, *Proceedings of the Physical Society*, 1944, **56**, 174.
4 K. Venkateswarlu, A. Chandra Bose and N. Rameshbabu, *Physica B: Condensed Matter*, 2010, **405**, 4256-4261.
5 A. Monshi, M. R. Foroughi and M. R. Monshi, *World Journal of Nano Science and Engineering*, 2012, **2**, 154.
6 H. Rietveld, *Journal of Applied Crystallography*, 1969, **2**, 65-71.
7 L. Lutterotti and P. Scardi, *Journal of Applied Crystallography*, 1990, **23**, 246-252.
8 M. Fadoni and L. Lucarelli, *Studies in Surface Science and Catalysis*, 1999, **120**, 177-225.